Blackbox Optimization for Aircraft Engine Blades With Contact Interfaces

Julien Lainé, Elsa Piollet, Florence Nyssen, Alain Batailly

▶ **To cite this version:**

Julien Lainé, Elsa Piollet, Florence Nyssen, Alain Batailly. Blackbox Optimization for Aircraft Engine Blades With Contact Interfaces. Journal of Engineering for Gas Turbines and Power, 2019, 141 (6), pp.061016. 10.1115/1.4042808 . hal-02059582v2

HAL Id: hal-02059582
https://hal.science/hal-02059582v2

Submitted on 7 May 2019

HAL is a multi-disciplinary open access archive for the deposit and dissemination of scientific research documents, whether they are published or not. The documents may come from teaching and research institutions in France or abroad, or from public or private research centers.

L'archive ouverte pluridisciplinaire **HAL**, est destinée au dépôt et à la diffusion de documents scientifiques de niveau recherche, publiés ou non, émanant des établissements d'enseignement et de recherche français ou étrangers, des laboratoires publics ou privés.

Blackbox optimization for aircraft engine blades with contact interfaces

Julien Lainé[1], Elsa Piollet[1], Florence Nyssen[1], Alain Batailly[1]

Abstract

In modern aircraft engines, reduced operating clearances between rotating blade tips and the surrounding casing increase the risk of blade/casing structural contacts, which may lead to high blade vibration levels. Therefore, structural contacts must now be accounted for as early as in the engine design stage. As the vibrations resulting from contact are intrinsically nonlinear, direct optimization of blade shapes based on vibration simulation is not realistic in an industrial context. A recent study on a blade featuring significantly lower vibration levels following contact event identified a potential criterion to estimate a blade sensitivity to contact interactions. This criterion is based on the notion of dynamic clearance, a quantity describing the evolution of the blade/casing clearance as the blade vibrates along one of its free-vibration modes. This paper presents an optimization procedure which minimizes the dynamic clearance as a first step toward the integration of structural criteria in blade design. A dedicated blade geometry parameterization is introduced to allow for an efficient optimization of the blade shape. The optimization procedure is applied to the three-dimensional properties of two different blades. In both cases, initial and optimized blades are compared by means of an in-house numerical tool dedicated to the simulation of structural contact events with a surrounding casing. The simulations focus on rubbing phenomena, involving the vibration of a single blade. Simulation results show a significant reduction of vibration levels following contact interactions for the optimized blades. Critical speeds related to the mode on which the dynamic clearance is computed are successfully eliminated by the blade shape optimization. For the investigated blade geometries, backward sweep and backward lean angles are associated with reduced contact interactions compared to forward sweep and forward lean angles.

Keywords

rotor/stator interaction; blackbox optimization; blade design; nonlinear dynamics; dynamic clearance

1 - Department of Mechanical Engineering, École Polytechnique de Montréal, P.O. Box 6079, Succ. Centre-Ville, Montréal, Québec, Canada H3C 3A7

Optimisation boîte noire d'aubes de moteur d'avion avec des interfaces de contact

Julien Lainé[1], Elsa Piollet[1], Florence Nyssen[1], Alain Batailly[1]

Résumé

Dans les moteurs d'avions récents, la réduction des jeux entre l'extrémité des aubes en rotation et le carter environnant augmente le risque de contacts structurels entre les aubes et le carter, ce qui peut conduire à de hauts niveaux de vibrations. Les contacts structurels doivent donc désormais être pris en compte dès la conception du moteur. Comme les vibrations générées par un contact sont intrinsèquement non-linéaires, une optimisation directe de la géométrie des aubes basée sur une simulation vibratoire n'est pas réaliste dans un contexte industriel. L'étude récente d'une aube présentant des niveaux de vibration significativement réduits après une interaction de contact a permis d'identifier un critère possible pour estimer la criticité d'une aube par rapport aux interactions de contact. Ce critère est basé sur la notion de jeu dynamique, une quantité qui décrit l'évolution du jeu aube/carter lorsque l'aube vibre selon l'un de ses modes propres. Ce papier présente une procédure d'optimisation qui minimise le jeu dynamique, et qui représente une première étape vers l'intégration de critères structurels dans la conception d'aubes. Une paramétrisation de l'aube est introduite pour permettre l'optimisation efficace de la géométrie de l'aube. La procédure d'optimisation est appliquée aux propriétés tridimentionnelles de deux aubes différentes. Dans les deux cas, les aubes initiales et optimisées sont comparées à l'aide d'un outil numérique interne dédié à la simulation de contacts avec le carter environnant. Les simulations se concentrent sur le phénomène de frottement aube/carter (*rubbing*) qui implique la vibration d'une seule aube. Les résultats de simulation montrent une réduction significative des niveaux de vibration suite à une interaction de contact pour les aubes optimisées. Les vitesses critiques associées au mode pour lequel le jeu dynamique est calculé sont éliminées avec succès par l'optimisation de l'aube. Pour les géométries d'aube étudiées, un angle de flèche vers l'aval et un angle d'inclinaison contre le sens de rotation sont associés à des interactions de contact réduites par rapport à un angle de flèche vers l'amont et un angle d'inclinaison dans le sens de rotation.

Mots-clés

interaction rotor/stator; optimisation boîte noire; conception d'aube; dynamique non-linéaire; jeu dynamique

1 - Département de génie mécanique, École Polytechnique de Montréal, P.O. Box 6079, Succ. Centre-Ville, Montréal, Québec, Canada H3C 3A7

Nomenclature

Letters and symbols

A	profile area
R	outer blade radius
Γ	optimization constraints
Ω	angular speed
$\bar{d}$	mean distance between data points and model
$\boldsymbol{\phi}$	modal displacement field
δp	perimeter difference
δ	amplitude coefficient of the blade vibration
$\mathbf{K}$	stiffness matrix
$\mathbf{f}$	force vector
$\mathbf{u}$	displacement field
θ	iteration index
$\mathbf{x}$, $\mathbf{y}$, $\mathbf{z}$	cartesian coordinates
ζ	displacement criterion
c_{d}	dynamic clearance
f	objective-function
s	similarity score

Acronyms

1B	first bending mode
1T	first torsional mode
2B	second bending mode
LE	leading edge
TE	trailing edge

Subscripts and superscripts

i	profile index, $i = \mathrm{I}, \mathrm{II}, \mathrm{III}$
b	blade
p	profile

1 Introduction

The reduction of fuel consumption is a driving factor in the design of turbomachinery, both for environmental and economic reasons. As the aerodynamic performance of rotating blades is one of the key parameters in the overall engine efficiency, it is one of the main focuses of rotor design, relating to fan [1], compressor [2, 3, 4] or turbine [5, 6] stages. In particular, tighter operating clearances are desirable between rotating blades and the surrounding casing to reduce tip losses [7]. Blade shapes can also be optimized to increase aerodynamic efficiency or pressure ratio, for example, through the application of three-dimensional (3D) tilt angles [8, 9].

In a linear context, the consequences of blade design modifications on its dynamics may be easily quantified with a modal analysis and access to its basic properties such as the variation of mass. Multidisciplinary optimizations can also be carried out by combining aerodynamic criteria with structural criteria such as static stresses or vibration modes [10]. In a nonlinear context, however, the aftermath of the redesign may have a strong impact on the vibration behaviour of the blade which, in turn, might yield a reduced lifespan. The lack of versatile theories for the analysis of nonlinear mechanical systems makes it particularly arduous for designers to quantify the impact of redesign operations on the blade's dynamics.

Furthermore, the drive toward tighter clearances unavoidably increases the risks of structural contacts between the blades and the casing. Thus, such interactions must now be taken into account in the engine normal operating conditions. These intrinsically nonlinear contact interactions may result in damaging vibrations due to rubbing phenomena (a single blade impacting the casing repeatedly)[11, 12], modal interaction between the full bladed disk and the casing [13], or even shaft motions such as whirl motions [14, 15]. It therefore becomes critical for designers to be able to accurately assess the level of sensitivity of a given blade to structural contacts as early as in the design stage in order to avoid costly design iterations [16]. This requires the definition of new design criteria in line with nonlinear dynamics considerations.

A potential criterion was identified recently through the redesign of a blade following structural contact events [17]. Investigations on the resulting blades [18] underlined that the redesigned blade featuring lower vibration response to contact interactions essentially differed from the original blade design with respect to its ability to maintain an almost constant blade/casing clearance as it vibrated along its first bending mode. The evolution of blade/casing clearance during modal vibration was called the clearance consumption [18]. In this article, for the sake of clarity, clearance consumption is replaced by its opposite ($(-1)\times$clearance consumption), and is named the *dynamic clearance*. When the dynamic clearance is positive, clearance increases, and vice versa. For a vibrating blade, the total clearance is the sum of the clearance at rest and its dynamic clearance.

The present work seeks to develop an optimization procedure based on a single criterion related to a blade's dynamic clearance. It aims at assessing the relevance of the notion of dynamic clearance as a way to quantify a blade's sensitivity to structural contacts occuring along its chord, with the surrounding casing. This procedure is a first step toward the inclusion of nonlinear dynamics related criteria in a multidisciplinary optimization procedure dedicated to aircraft engine bladed components. The originality of this work lies in the possible use of a criterion that can be obtained through linear computation, while predicting the blade sensitivity to a nonlinear phenomenon. The relevance of the proposed optimization criterion is here assessed from a purely structural point of view. For that reason, and as a first approximation, aerodynamic considerations are intentionally left aside. Moreover, only contact interactions involving a single blade (rubbing phenomena) are considered.

In the second section, details are given on the notion of dynamic clearance. In the third section, an original blade geometry parameterization is proposed to serve as a basis for the optimization of blade geometries. The automated optimization procedure is then presented in the fourth section. Section five describes the analysis framework employed to obtain relevant information from the application of the procedure. Finally, in the sixth section, two different blade geometries are optimized with respect to their 3D parameters. Initial and resulting blades are compared through nonlinear simulations of contact interactions. These simulations show that minimizing the dynamic clearance for the first bending mode leads to a successful reduction of interactions related to this mode.

Note: in this article, $\mathbf{z}$ is the rotation axis of all investigated blades.

2 Dynamic clearance

2.1 Definition

When designing a blade, the clearance between the blade and the casing can be predicted for a given speed, by taking into account phenomena such as centrifugal effects or thermal expansion. The resulting clearance for a given speed is referred to as

static clearance in this section. Vibrations of the blade modify the actual clearance as the blade gets closer or farther from the casing. This variation of clearance around the static clearance is called the *dynamic clearance* in the present paper.

More specifically, the dynamic clearance is defined at a given location along the blade-tip as the evolution of blade/ casing clearance as the blade vibrates along one of its free vibration modes, typically the first bending mode (1B) or the first torsional mode (1T). Associated dynamic clearances are respectively denoted $c_{\mathrm{d}}^{1\mathrm{B}}$ and $c_{\mathrm{d}}^{1\mathrm{T}}$. In this article, all dynamic clearances are computed at the blade leading edge (LE) and are relative to the first bending mode—which corresponds to the first free-vibration mode of all investigated blades. Indeed, the leading edge area—typically the stiffer area of the blade-tip for compressor blades—was identified by the authors as key in the emergence of divergent vibratory phenomena following structural contact events in previous publications [18].

As the blade vibrates, the actual blade/casing clearance is the sum of the static clearance and the dynamic clearance. A negative dynamic clearance indicates that the clearance has decreased, and therefore the blade is closer to the casing. Conversely, a positive dynamic clearance implies that the blade/ casing clearance has increased. The amplitude of the dynamic clearance depends on the amplitude of vibration of the blade for the mode of interest. To compare the dynamic clearances of two blades, an admissible domain of vibration must be defined. In this article, the admissible domain is defined by a maximum displacement criterion ζ related to the blade's leading edge tangential displacement (along the $\mathbf{x}$ direction, see Fig. 1):

$$|u_{\mathrm{LE},t}\left(\Omega=0\right)| \leq \zeta \tag{1}$$

The value of ζ is discussed later in this article.

2.2 Computation

A modal analysis of the blade finite element model yields the blade's first bending mode $\boldsymbol{\phi}_{1\mathrm{B}}$. This mode is scaled in order to reach the limit of the aforementioned criterion:

$$u_{\mathrm{LE},t} = \pm\zeta \tag{2}$$

A static computation then allows retrieving the force vector $\mathbf{f}_{1\mathrm{B}}$ which would yield the scaled displacement field $\tilde{\boldsymbol{\phi}}_{1\mathrm{B}}$:

$$\mathbf{f}_{1\mathrm{B}} = \mathbf{K}_{\mathrm{b}}\tilde{\boldsymbol{\phi}}_{1\mathrm{B}} \tag{3}$$

where $\mathbf{K}_{\mathrm{b}}$ is the blade's stiffness matrix. Then, several displacement fields $\mathbf{u}_{1\mathrm{B}}$ are computed:

$$\mathbf{u}_{1\mathrm{B}}(\delta) = \delta\mathbf{K}_{\mathrm{b}}^{-1}\mathbf{f}_{1\mathrm{B}} \tag{4}$$

where δ is a given parameter comprised between -1 and 1. The static analysis to obtain the displacement field may be linear or nonlinear. In the case of a linear computation, the resulting displacement field is simply the scaled displacement field $\tilde{\boldsymbol{\phi}}_{1\mathrm{B}}$, but additional computations are required for the nonlinear case.

For each value of δ, the dynamic clearance $c_{\mathrm{d}}\left(\delta\right)$ is then calculated as the difference between the blade radius at rest R_0 and the blade radius $R\left(\delta\right)$ corresponding to displacement field $\mathbf{u}_{1\mathrm{B}}\left(\delta\right)$, as illustrated on Fig.1:

$$c_{\mathrm{d}}\left(\delta\right) = R_0 - R\left(\delta\right) \tag{5}$$

$$R(\delta) = \sqrt{\left(x\left(\delta\right)\right)^2 + \left(y\left(\delta\right)\right)^2} \tag{6}$$

where $x\left(\delta\right)$ and $y\left(\delta\right)$ are the cartesian coordinates of the leading edge extracted from the blade displacement field $\mathbf{u}_{1\mathrm{B}}(\delta)$. Figure 2 illustrates the dynamic clearance as a function of δ. One may note that, depending on the casing conicity, the computation of the dynamic clearance could involve the axial displacement of the blade, as illustrated on Fig. 3. In the present study, all casings are assumed perfectly cylindrical for the sake of simplicity.

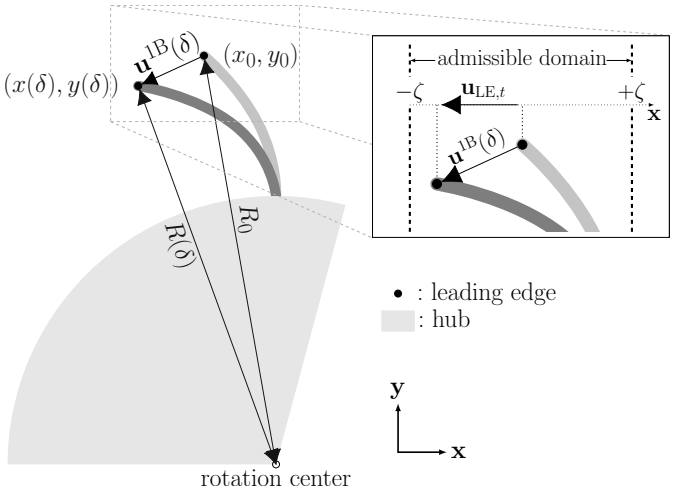

Figure 1. blade radius calculation, blade at rest (——) and vibrating blade (——)

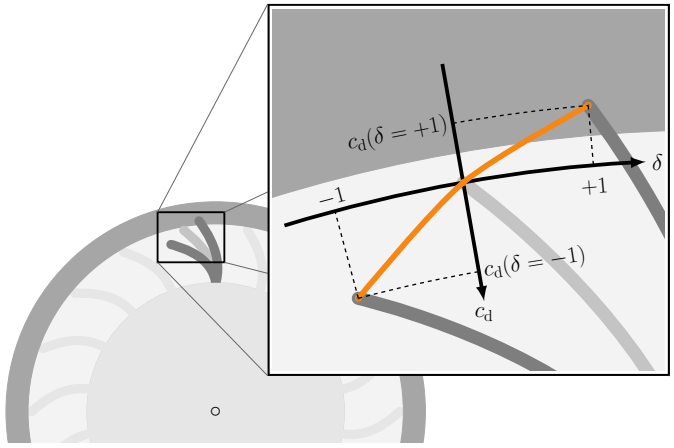

Figure 2. schematic representation of the dynamic clearance (——), blade at rest (——) and vibrating blade (——)

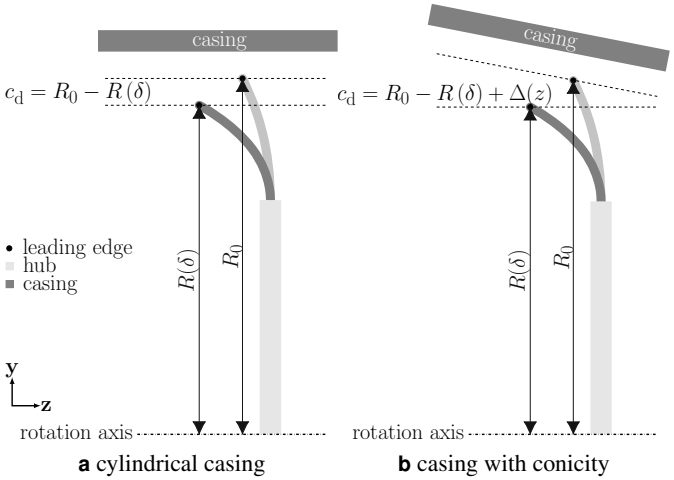

Figure 3. effect of casing conicity on the computation of dynamic clearance, blade at rest (——) and vibrating blade (——)

3 Blade modeling

In order to be able to optimize a blade shape, it is first necessary to define a parameterization of its geometry. This parameterization must rely on a limited set of parameters for the sake of efficiency. Yet, it must be flexible enough to represent realistic blade geometries. An explicit parametric model of a blade is created for the purpose of this study. As illustrated in Fig. 4, the blade is described through three two-dimensional profiles, representing the cross-section of the blade across its span (root I, mid-span II and tip III). The choice of three profiles to describe the full blade is consistent with previous works on blade design [8]. The profile positions and orientations are given by the stacking law (—), which spawns the three-dimensional shape of the blade.

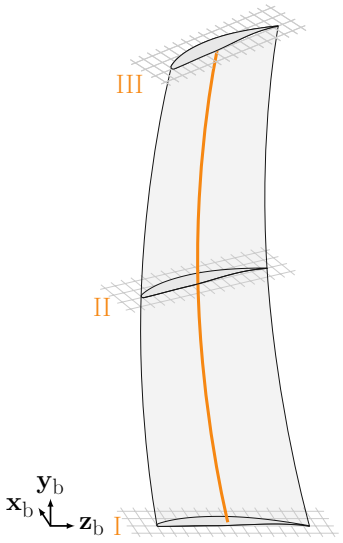

Figure 4. blade model with associated profiles (□) and stacking line (—)

3.1 Profile parameterization

3.1.1 Definition

A profile is described in its own local coordinate system $(\mathbf{x}_p^i, \mathbf{y}_p^i, \mathbf{z}_p^i)$, for $i = \mathrm{I}, \mathrm{II}, \mathrm{III}$. In this study, profiles are planar and defined in the plane $(\mathbf{x}_p^i, \mathbf{z}_p^i)$. In the present paper, the direction $\mathbf{z}_p^i$ is the chordwise direction of the profile, but the model allows other orientations of the profile. The proposed modeling of blade profiles, depicted in Fig. 5, builds on the work of Pritchard [19] and Cho [20]. The model relies on the use of two elliptical arcs for the leading edge, one circular arc for the trailing edge, and two spline curves for the representation of both the suction side and the pressure side. This model advantageously combines a smooth representation of pressure and suction sides with an independent formulation of each side. It can easily be implemented within a CAD software and it will be shown that it is flexible enough to accurately represent a large variety of existing blade profiles.

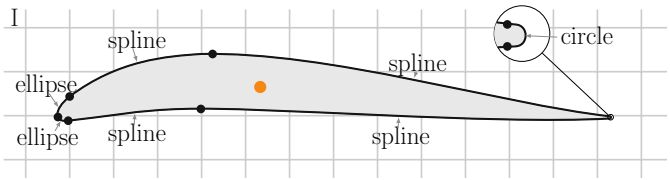

Figure 5. profile description with center of gravity (●)

As is, the model contains a total of 16 parameters. However, in order to improve the numerical efficacy of the procedure, the ellipse axis ratios are arbitrarily fixed to 2 for this study. In the end, the model can be entirely parameterized with only 14 parameters while ensuring $\mathcal{C}^1$-continuity. Figure 6 details these 14 parameters.

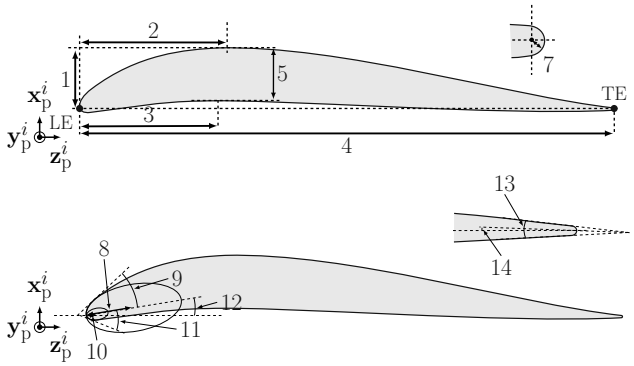

(1) suction peak point (x coordinate)
(2) suction peak point (z coordinate)
(3) pression peak point (z coordinate)
(4) axial chord = $z_{\mathrm{T}} - z_{\mathrm{L}}$
(5) maximum thickness
(6) tangential chord = $x_{\mathrm{T}} - x_{\mathrm{L}}$
(7) trailing edge radius
(8) major radius upper ellipse
(9) inlet upper wedge angle
(10) major radius lower ellipse
(11) inlet lower wedge angle
(12) blade inlet angle
(13) outlet wedge angle
(14) blade outlet angle

Figure 6. profile parameters, LE: leading edge at origin and TE: trailing edge

3.1.2 Profile reconstruction

In the literature, profiles are often provided as a list of data points or coordinates [21, 22, 23]. In this case, a reconstruction of the profiles is needed to obtain the 14 parameters from the discrete points. To this end, an optimization procedure has been designed in order to identify the optimal value of each of the 14 parameters for each profile of interest. This procedure is twofold:

first step: all parameters that may be obtained directly from the profile coordinates given in the literature are computed:

- (1) and (2): suction peak coordinates,
- (4): axial chord,
- (6): tangential chord.

second step: remaining parameters are identified by an optimization algorithm[1] in order to fit the blade profile with the given coordinates. This fitting is estimated by a *similarity score* s calculated with: (1) the mean distance $\bar{d}$ between the data points and the computed profile and, (2) the perimeters difference δp:

$$s = 1 - (0.9\bar{d} + 0.1\delta p) \tag{7}$$

The closer s is to 1, the better the approximation of the profile. The weights applied to $\bar{d}$ and δp were chosen empirically. Figure 7 shows the application of this criterion on an elliptical shape that is approximated using the proposed set of parameters. Four consecutive iterations of the optimization procedure are depicted, they feature a similarity score ranging from $s = -0.22$ to $s = 0.944$. The last iteration with $s = 0.944$, see Fig. 7d, provides a satisfying match with the targetted shape. For each iteration, the relative area error is also displayed, this value indicates the relative error between the area of the targetted ellipse and the area of the computed profile. Contrary to the relative area error, the similarity score s accounts for local mismatch between the optimized profile and given data points thus making it more relevant for estimating the quality of the fitting. As an example, Figs. 7b, 7c and 7d feature almost identical relative area error while the similarity score decreases significantly as the accuracy of the fitting increases. The same observation could be made on the use of the mean distance $\bar{d}$ only, which is not sufficient for profiles with a low point density, hence the use of a similarity score combining $\bar{d}$ and δp.

3.1.3 Application

The versatility of the proposed model is assessed by applying it to well-known existing blade profiles that may be found in the literature as a list of data points or coordinates. The fitting of 6 compressor blade profiles (two NACA profiles as defined

[1] The employed optimization strategy relies on the NOMAD software presented in details in the following of the article.

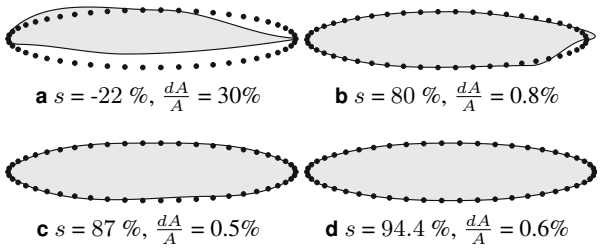

Figure 7. similarity score and relative area errors computed for an elliptical shape (●) and four iterated sets of parameters (□)

in [21], 3 profiles from the rotor 37 blade given in [22] and the man ghh 1-s1 profile from [23]) with the proposed model is depicted in Fig. 8. For each profile, there is an excellent visual match between the parameterized model and the data points given in the literature. This observation is confirmed by the very good similarity score obtained for each profile. These results underline that the proposed model can accurately represent a large variety of blade profiles thus emphasizing the versatility of the proposed parameterization.

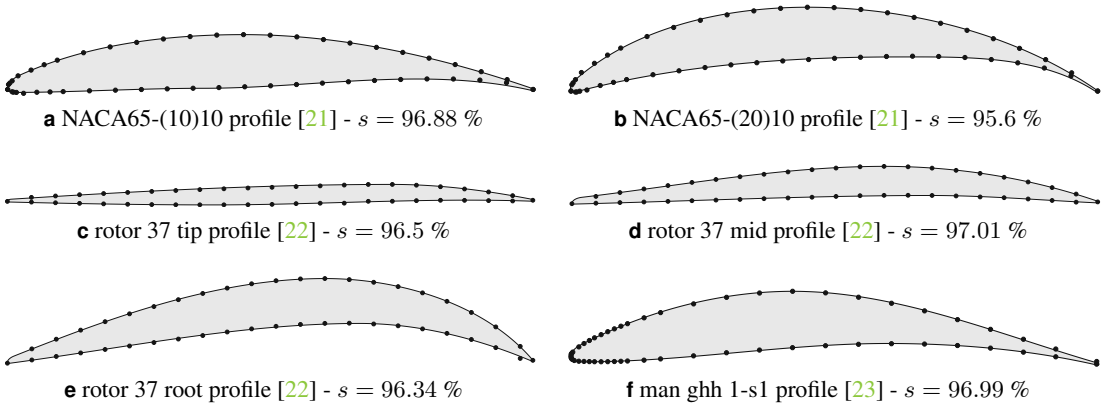

Figure 8. superimposition of 6 compressor blade profiles as given in the literature (●) and the associated parameterized profiles (□)

3.2 3D parameters

As described in Fig. 4, the full blade model is obtained by first defining its three profiles using the parameterization described above. Then, the following steps are:

1. the centers of gravity of the three profiles are positioned in their respective planes,
2. the profiles are oriented with respect to each other,
3. the blade is extruded from one profile to the other according to the stacking law,
4. the whole blade is oriented with respect to the rotor axis.

Profile positioning and orientation, as well as blade extrusion, are guided by the so-called stacking law, which is composed of two elements: (1) the stacking line that connects the centers of gravity of all profiles and, (2) the stagger angle that defines the relative orientation between the profiles. The whole blade orientation is controlled by the angle of incidence. Subsections 3.2.1 and 3.2.2 detail the seven parameters used for the full blade definition.

3.2.1 Stacking line

The three profiles of the blade are defined in three parallel planes equally distributed along the blade height. As shown in Fig. 9, the hub radius (15) and the blade height (16) give the radial positions of the root profile and the tip profile. The stacking line gives the positions of the profiles within their plane of definition. The positions of the three centers of gravity are adjusted through two angles, the sweep angle (17) and the lean angle (18) and through a curvature given by the bowed distance (19).

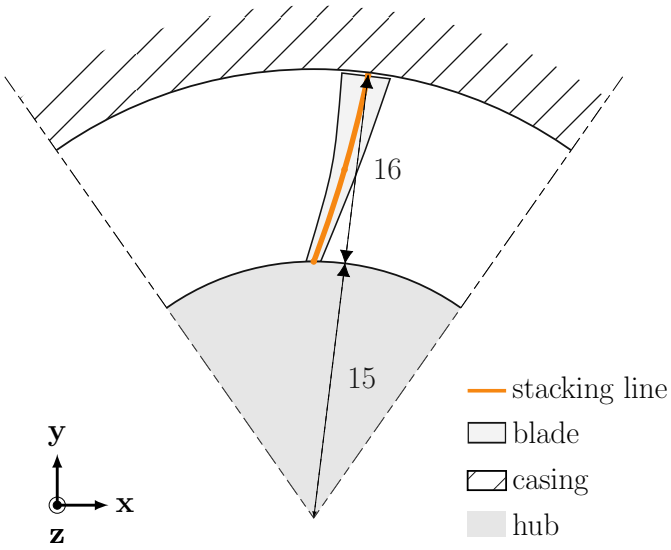

a rear view of the blade/hub assembly within a casing

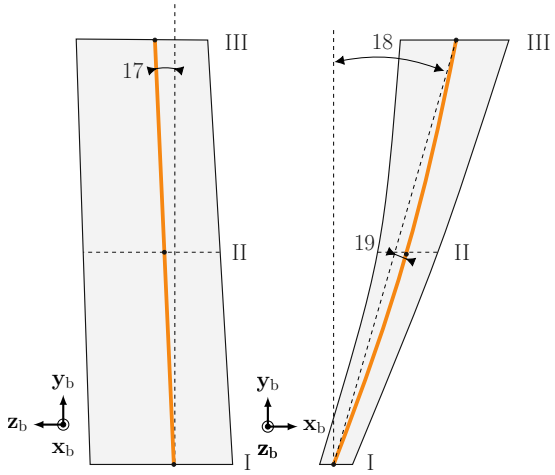

b side view of the blade **c** rear view of the blade

(15) hub radius (17) sweep angle (19) bowed distance
(16) blade height (18) lean angle

Figure 9. stacking line parameterization with 2 angles and 3 lengths

The stacking line is a cubic spline interpolating the positions of the centers of gravity of the three profiles. The parameters are defined in the blade coordinate system ($\mathbf{x}_b$, $\mathbf{y}_b$, $\mathbf{z}_b$): as the root profile coordinate system is the same as the blade coordinate system, the sweep is the chordwise or "true" sweep [24] for the root. The lean angle is perpendicular to the chordline of the root.

3.2.2 Angle of incidence and stagger angle

The angle of incidence (20), illustrated in Fig. 10, gives the orientation of the blade with respect to the rotor axis. The stagger angle (21) allows for a change in the incidence angle along the blade span, therefore twisting the blade around the radial

direction $\mathbf{y}$. It is defined as the angle between the root and tip profiles.

In the end, $3 \times 14 + 7 = \mathbf{49}$ parameters are needed to build the whole blade: 14 parameters for each profile (see Fig. 6) and 7 parameters for the 3D extrusion (as shown in Figs. 9 and 10).

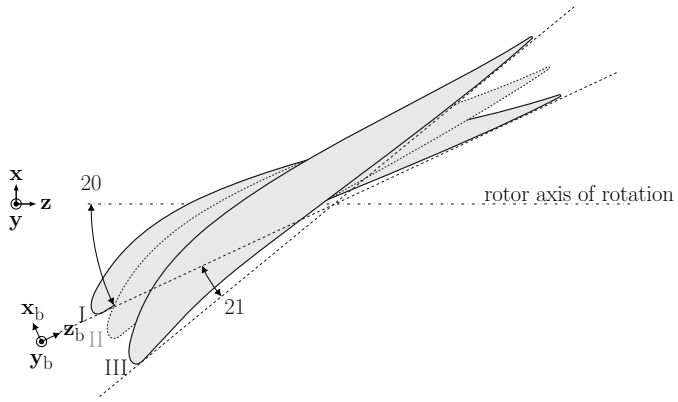

(20) angle of incidence (21) stagger angle

Figure 10. representation of the stagger angle and the angle of incidence

4 Optimization procedure

The goal of the optimization procedure is to modify a blade geometry in order to minimize the amplitude of the dynamic clearance at the leading edge as the blade vibrates along its first bending mode. Based on the evolution of the dynamic clearance for a given blade, see graph (——) in Fig. 2 for instance, the procedure aims at flattening the graph with respect to the abscissa axis, *i.e.* it minimizes the objective function defined by:

$$f(\theta) = \max_{\delta \in \{-1,1\}} (c_{\mathrm{d}}(\delta)) \tag{8}$$

at each iteration step θ.

Constraint functions are also used in the optimization procedure to maintain a realistic geometry. In future work, such constraints will allow for the design of industrially relevant bladed components, by including aerodynamic considerations for example. In the present study, a simple set of constraints is used to demonstrate the principle of the procedure with a structural focus only. Therefore, the optimization features three constraints Γ_i, $i = \mathrm{I}, \mathrm{II}, \mathrm{III}$ which keep the area of the three profiles within a $\pm 10\%$ range around the initial areas in order to preserve realistic blade profiles:

$$\Gamma_i = -0.1 + \frac{|A_i - A_{i,0}|}{A_{i,0}} \tag{9}$$

where A_i stands for the area of the iterated profile i, and $A_{i,0}$ stands for the area of the initial profile i (constraints that are negative are considered satisfied by the employed optimization algorithm).

4.1 Algorithm

The optimization is conducted with the NOMAD software and its Mesh Adaptive Direct Search (MADS) algorithm [25, 26]. NOMAD is a blackbox optimization software, which means that the objective function and the constraints are given at each iteration by an external computer code: the *blackbox*. NOMAD's optimization algorithm is totally independent from the blackbox internal operations and only uses the values of the objective function and the constraints to determine the next iteration. MADS algorithm and NOMAD software have been applied successfully to diverse industrial applications [27, 28].

One may note that proof of convergence toward an optimum has only been demonstrated for specific objective function characteristics. In the present case, the nature of the objective function does not allow proving convergence toward an optimum.

Therefore, the results given by the optimization procedure cannot be considered as optima. In the following, when the term "optimized blade" is used, it refers to the blade geometry obtained at the end of the optimization procedure. It does not imply that the result is optimal, as this cannot yet be proven mathematically.

4.2 Inside the blackbox

Figure 11 depicts an iteration θ of the optimization procedure, during which the objective function and the constraints are computed. At the beginning of the iteration step, NOMAD provides 49 parameters to the blackbox. These 49 parameters are used to build the blade CAD model with the SALOME software package [29], an open-source platform that provides both CAD and meshing tools. Within SALOME, the computation of each profile area allows estimating the three constraints $\Gamma_i(\theta)$. The CAD model is then meshed with hexahedral elements with two fixed parameters: (1) the number of elements along the blade thickness and, (2) the total number of elements in the mesh. The resulting finite element mesh is exported, translated and then read by the commercial finite element software Samcef (LMS Samtech). Samcef is used to compute the blade dynamic clearance, specifically $c_{\mathrm{d}}(\delta = +1)$ and $c_{\mathrm{d}}(\delta = -1)$, through modal and static computations, as described in Eq. (2) to (5). From these two values, the objective function $f(\theta)$ defined in Eq. (8) may then be computed. The value of $f(\theta)$ and the three constraints $\Gamma_i(\theta)$ are finally returned to NOMAD that will provide a new set of design parameters for iteration $\theta + 1$.

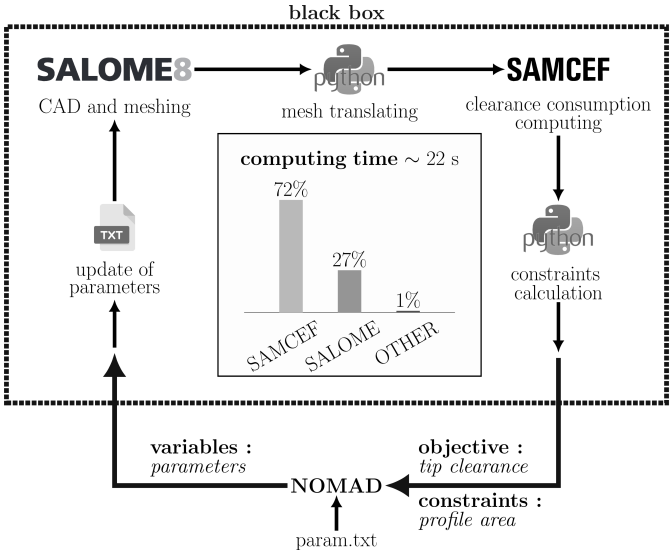

Figure 11. description of one iteration of the procedure

4.3 Validity of linear computations

Dynamic clearance can be obtained either from linear or nonlinear static finite element computations. Nonlinear computations provide more accurate results, but the use of a linear solver allows for significantly lower computation cost, which is crucial in an optimization context when the objective function has to be computed repeatedly. To be able to use linear computations, one must ensure that minimizing the linearly computed dynamic clearance is consistent with the minimization of the nonlinearly computed dynamic clearance.

A test blade is used to illustrate the effect of both computation types on the obtained dynamic clearance. This test blade is composed of three NACA65-(10)10 profiles, along with the design parameters given in Tab. 1. Figure 12 shows the dynamic clearance at the leading edge of the blade for the first bending mode, computed with both linear (——) and nonlinear (- - -) solvers. Calculations are run with a 5000 element mesh of the blade. As an example, a fairly large value of the maximum tangential displacement criterion ζ is considered: $\zeta = 25$ mm. Such displacement corresponds to 17 % of the blade height. As could be expected, for small values of δ, linear and nonlinear computations yield similar results: both graphs (——) and (- - -) are superimposed. For larger values of δ, both computations yield different results, however both positive and negative dynamic clearances obtained through linear computation are representative of the trend observed with the nonlinear

parameter	value
hub radius (**15**)	350 mm
blade height (**16**)	150 mm
sweep angle (**17**)	-7.5°
lean angle (**18**)	20°
bowed distance (**19**)	20 mm
angle of incidence (**20**)	0°
stagger angle (**21**)	10°

Table 1. 3D parameters of the example blade

computation. Therefore, in this case, decreasing the linear dynamic clearance will also decrease the nonlinear dynamic clearance. Nonetheless, for all applications presented in this article, both linear and nonlinear computations are compared for the initial and optimized blades. Also ζ is set to $\zeta = 2$ mm, corresponding to $\delta = 0.08$ in Fig. 12.

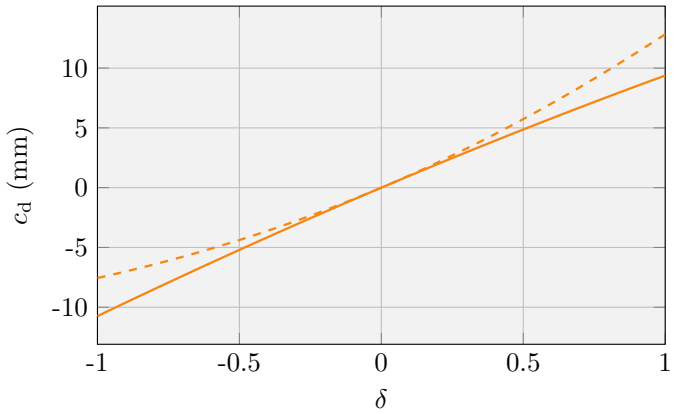

Figure 12. dynamic clearance of the blade for $\zeta = 25$ mm with linear (——) and nonlinear (- - -) solvers

4.4 Space convergence

As mentioned in the blackbox description, two parameters are fixed for the blade meshing: the total number of elements in the mesh and the number of elements over the blade thickness. It is standard practice in the industry to use at least two elements over the blade thickness. For this study, this number is set to four. The total number of elements is selected from a spatial convergence study on the test blade presented in the section 4.3. Figure 13 shows the evolution of the maximum value of the dynamic clearance depending on the total number of elements. The calculations converge rapidly: for 500 elements and over, the value of dynamic clearance remains almost identical from a mesh to another. In the following, 1000 elements are used for all finite element meshes.

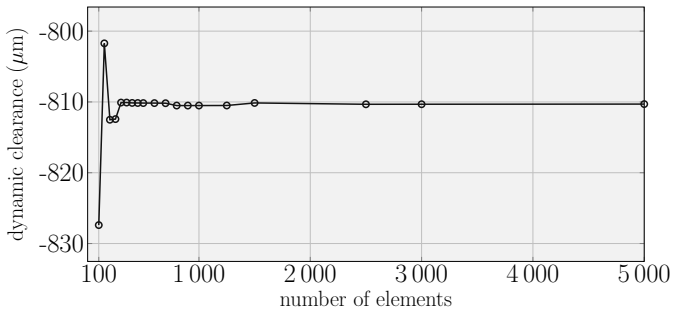

Figure 13. convergence of the maximum value of the blade's dynamic clearance with respect to the number of finite elements

5 Analysis framework

5.1 Scope of investigation

The optimization procedure is applied to two blade geometries, with a focus on the effect of 3D parameters (parameters (15) to (21)). The goals of this application are listed below:

1. to demonstrate the ability of the procedure to reduce the dynamic clearance through blade shape optimization;
2. to assess the relevance of maximum dynamic clearance as a criterion to reduce blade sensitivity to contact events;
3. to provide a detailed analysis of the differences between initial blades and optimized blades through nonlinear contact simulations;
4. to obtain first tendencies in the effect of 3D parameters on the sensitivity of blades with respect to contact interactions.

The first blade is a simplified blade defined by three identical NACA65-(10)10 profiles, from the NACA65 series [30]. The specificity of this blade, illustrated in Fig. 14, lies in the use of a positive sweep angle, based on the Full Forward Chordwise Swept (FFCS) design recommended in [7] to reduce the sensitivity of the blade aerodynamic performance to tip clearance. While forward sweeps have been investigated for their effect on aerodynamic properties of the blades [7, 8], they have not been evaluated regarding sensivity to contact events with the casing.

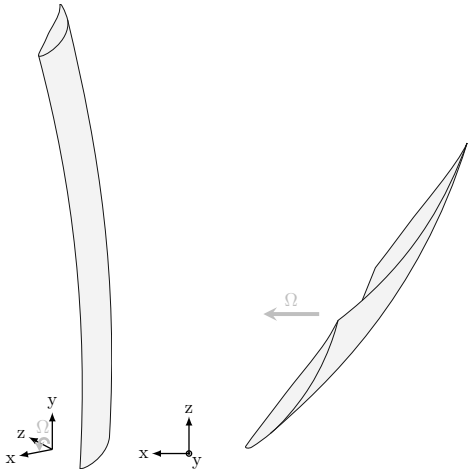

a side view **b** view from above

Figure 14. FFCS blade geometry

The second blade is a transonic compressor blade with a more realistic geometry. The 3D parameters are based on the geometry of the rotor 37, a NASA rotor widely used as a validation case for aerodynamic simulations [22, 31]. The hub profile is also set to fit with the hub section of the rotor 37, while the 2 other profiles are built as a homothety of this first profile. The homothetic ratio between the hub and tip profiles is 1.023 in the $\mathbf{z}_p$ direction and 0.3 in the $\mathbf{x}_p$ direction, which provides similar

profile areas and total volume compared to the original rotor 37. The corresponding geometry is visible in Fig. 15. For both optimizations, the 4 following stacking parameters are considered as optimization variables : the sweep angle (17), the lean angle (18), the bowed distance (19), and the stagger angle (21).

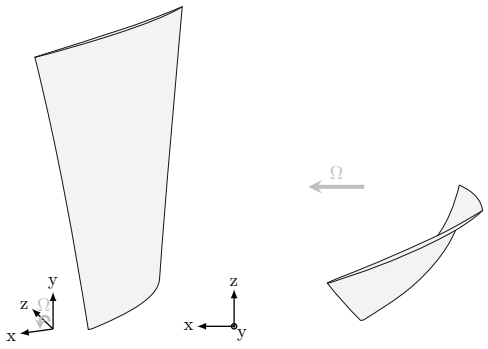

a side view **b** view from above

Figure 15. transonic blade geometry

5.2 Nonlinear simulations

The vibration properties of the initial and optimized blades are analyzed to assess if the obtained reduction in dynamic clearance actually corresponds to a reduced contact sensitivity. Two tools are used for this vibration analysis: the Campbell diagrams of the blades, and a numerical simulation of contact interactions. The former is a classical tool in rotordynamic analysis. It allows visualizing all the possible resonances in the system for a given set of modes and a given range of angular speeds. However, because contact phenomena are intrinsically nonlinear, it is impossible to predict which possible resonances will actually be observed in the system. This is why an in-house nonlinear simulation tool is employed in order to numerically assess blades sensitivity to structural contacts. The details of the numerical strategy were given in previous articles [12, 32] and only its main characteristics are recalled here for the sake of brevity. The simulation relies on an explicit time integration and contact events are managed through the use of Lagrange multipliers, which ensure that no penetration occurs between the blade and the casing. As is the case with industrial engines, the casing is coated with an abradable layer which allows softer contact interactions, as it may be easily worn off by the blade during contact events. Wear of the abradable coating is managed through the use of one-dimensional rod elements with a plastic constitutive law [33]. Only radial and tangential displacements of the blade tip are taken into account to evaluate the wear of the abradable elements. In the present case, both the dynamics of the casing and the disk are neglected, which leads to consider a perfectly rigid casing and to simulate only one blade, clamped at its root. Comparison with experiments on full-scale industrial bladed disks demonstrated that this strategy and assumptions led to realistic simulations for interaction events localized on a single blade [12, 32]. Other interactions such as modal interactions between the casing and the full bladed disk, which would include the casing and the disk dynamics, are out of the scope of this paper. This code is used to simulate 100 blade revolutions at a given angular speed, inside a deformed — yet perfectly rigid — casing, coated with a 5 mm thick abradable layer. Contact is initiated by applying an oval deformation to the casing which creates two privileged contact areas at angles $\frac{\pi}{2}$ and $\frac{3\pi}{2}$. Initial radial clearance is kept constant for all angular speeds, and centrifugal effects (centrifugal stiffening) are applied on the blades. Results of each numerical simulation feature the circumferential wear level of the abradable coating at the end of the simulation, as a function of the angular position on the casing. Simulations are run for a wide angular speed range in order to get the wear map, a two-dimensional representation of the wear level along the casing circumference at the end of a simulation for each angular speed. Convergence of the time integration procedure with respect to time and space was checked prior to running the interaction simulations but is not detailed in this article.

6 Results

6.1 Simplified FFCS blade

6.1.1 Initial blade

Simulations are carried out with an initial blade-tip/ abradable coating clearance of 0.5 mm, other relevant parameters are listed in Tab. 2. The associated wear map is depicted in Fig. 16 along with the blade's Campbell diagram. It is white where the abradable was not worn; grey areas indicate wear, with darker levels indicating higher levels of wear. The main wear areas for this blade are highlighted by the following symbols: ▲, ■, ●,♦ and ⬟. The number of wear lobes for each interaction speed is related to the engine order on which the phenomena appear. The comparison with the Campbell diagram then allows retrieving the vibration mode on which the interaction is predicted. For instance, interaction ■ features 4 lobes between 45 Hz and 50 Hz. Because the first bending mode intersects the 4th engine order around 42 Hz, the interaction may be attributed to this mode.

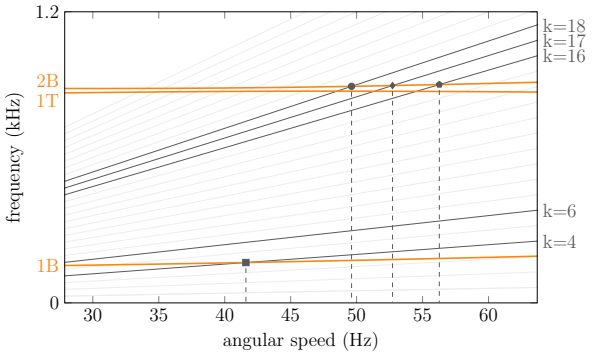

a Campbell diagram

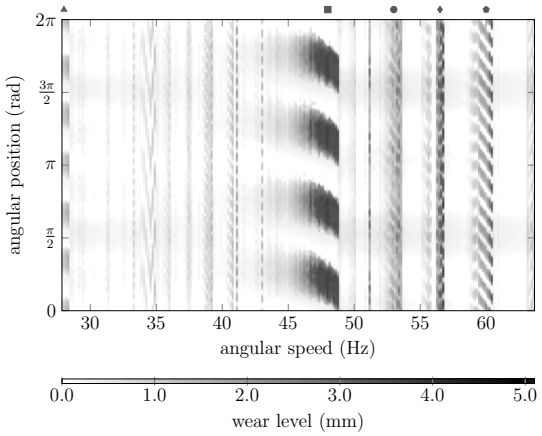

b wear map

Figure 16. initial FFCS blade analysis

One may note that the predicted interaction speeds found on the wear map are slightly higher than the critical speeds identified on the Campbell diagram. This is a consequence of the contact stiffening phenomenon that tends to increase a structure's eigenfrequencies when subject to contact. Interactions ●,♦,⬟ may not be clearly linked with a given mode because of the proximity of modes 1T or 2B, further investigations would be required to conclude but go beyond the scope of this study.

6.1.2 Optimization

As mentioned above, only four parameters are accounted for during this first optimization, namely the sweep angle (17), the lean angle (18), the bowed distance (19), and the stagger angle (21), see Tab. 3. Figure 17 shows the blade geometry evolution between the initial blade and the optimized one after 500 iterations. The optimized blade is swept in the opposite direction compared to the initial FFCS blade: it is now swept backward, in the downstream direction. The final geometric

parameter	initial	optimized
hub radius (**15**)	350 mm	350 mm
blade height (**16**)	150 mm	150 mm
sweep angle (**17**)	**25**°	**-10.50**°
lean angle (**18**)	**0**°	**-8.25**°
bowed distance (**19**)	**5 mm**	**0.75 mm**
angle of incidence (**20**)	36°	36°
stagger angle (**21**)	**0**°	**19.13**°

Table 2. initial and optimized parameters for the FFCS blade optimization; optimization variables are indicated in bold

parameter	lower limit	upper limit
sweep angle (**17**)	-30°	30°
lean angle (**18**)	-30°	30°
bowed distance (**19**)	0 mm	10 mm
stagger angle (**21**)	0°	45°

Table 3. optimization variable bounds

parameter values can be found in Tab. 2. The dynamic clearance improvement is displayed in Fig. 18. The maximum of dynamic clearance is lowered by 98.8% after the optimization, which shows that the optimization procedure works properly. The dynamic clearance obtained through nonlinear computations is also reduced.

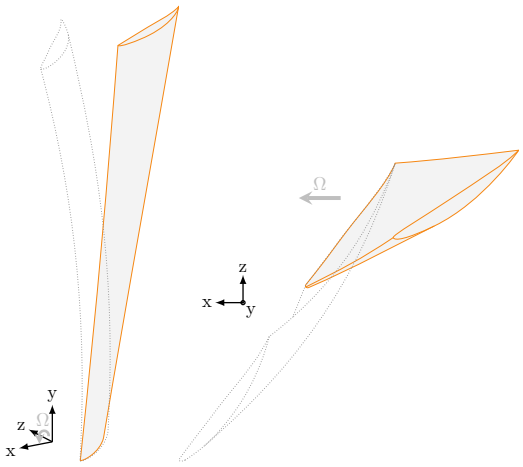

a side view **b** view from above

Figure 17. optimized FFCS blade geometry

6.1.3 Analysis

As the geometry is updated, eigenfrequencies of the blades are shifted. By comparison with Fig. 16a, the Campbell diagram depicted in Fig. 19a shows that the first bending mode and the first torsional mode frequencies are slightly higher than with the initial blade. The eigenfrequency of the second bending mode, on the other hand, is 300 Hz higher. Nevertheless, previous critical speeds remain located in the angular speed range of interest.

The resulting wear map, depicted in Fig. 19b, demonstrates great improvements regarding interactions as it features significantly less deep wear patterns. The first two bending mode interactions (▲ and ■), which can be seen in the initial wear map do not appear on the wear map of the optimized blade. Only four low amplitude interactions remain in the wear map of the optimized blade, and their number of lobes indicate that they are related to the first torsional mode.

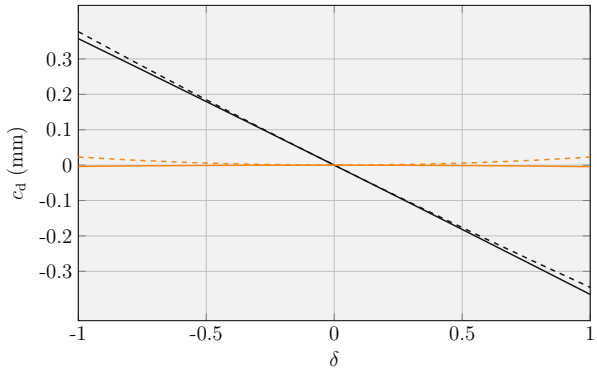

Figure 18. FFCS blade's dynamic clearance: initial (——) and optimized (——) blade (non-linear computations are depicted with dashed lines)

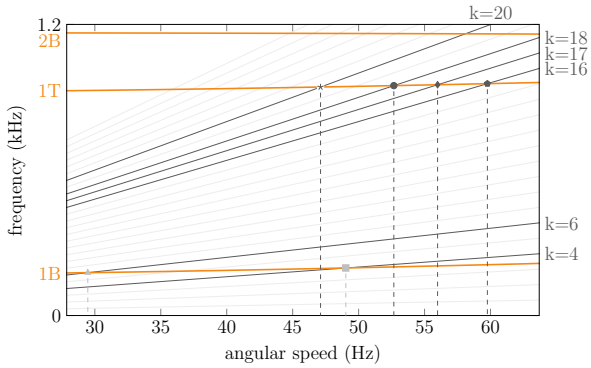

a Campbell diagram

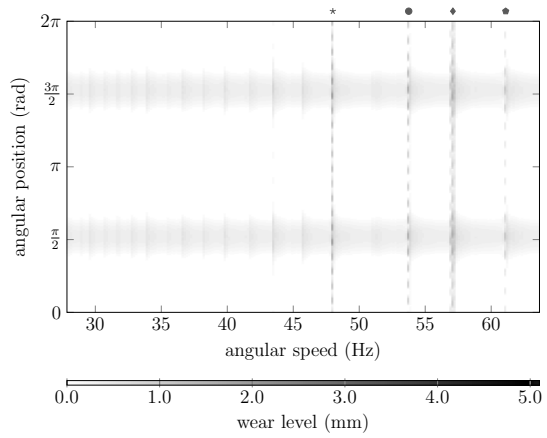

b wear map

Figure 19. optimized FFCS blade analysis

This application of the optimization procedure confirms its ability to reduce the maximum dynamic clearance through blade shape modification. It also demonstrates a patent desensitization of the blade to structural contacts. Moreover, these first results on 3D parameters show a much lower contact sensivity for the backward chord swept blade obtained by the optimization

process than for the initial forward chord swept blade. This seems to indicate that the FFCS design, while providing good aerodynamic results, may not be an eligible design option from a structural standpoint.

6.2 Transonic blade

6.2.1 Initial blade

Contact simulations are run with the same parameters as for the FFCS blade, except for the initial radial clearance, which is set to 0.1 mm. Other relevant parameters are listed in Tab. 4. All five main interaction speeds—noticeable in Fig. 20 and marked ⬟, ♦, ●, ■ and ▲—are related to an interaction with the first bending mode, for engine orders 4 to 8. Predicted interactions on higher modes feature very low amplitudes of vibration as evidenced by the lower depth of wear patterns in Fig. 20b.

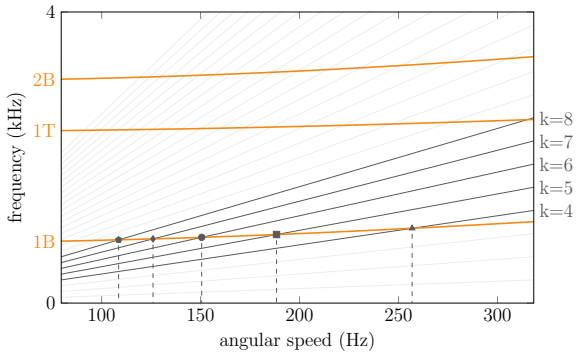

a Campbell diagram

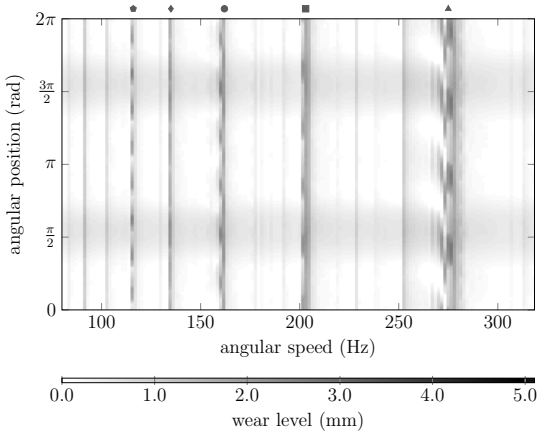

b wear map

Figure 20. initial transonic blade analysis

6.2.2 Optimization

Same as for the FFCS blade, the scope of the optimization focuses on four parameters (sweep angle (17), lean angle (18), bowed distance (19) and stagger angle (21)). As a first approximation, bounds considered for each of these parameters are identical to those given in Tab. 3. The optimization procedure yields the optimized blade pictured in Fig. 21, corresponding geometric parameters are listed in Tab. 4. One may note that both sweep and lean angles are increased while the bowed distance and stagger angles are reduced. As illustrated in Fig. 22, the optimization process yields a 91.6 % decrease in the maximum dynamic clearance.

parameter	initial	optimized
hub radius (**15**)	177 mm	177 mm
blade height (**16**)	75 mm	75 mm
sweep angle (**17**)	**0.2**°	**11.55**°
lean angle (**18**)	**4.20**°	**13.52** °
bowed distance (**19**)	**1.22 mm**	**0.41 mm**
angle of incidence (**20**)	36°	36°
stagger angle (**21**)	**28.85**°	**11.61**°

Table 4. initial and optimized parameters for the transonic blade optimization; optimization variables are indicated in bold

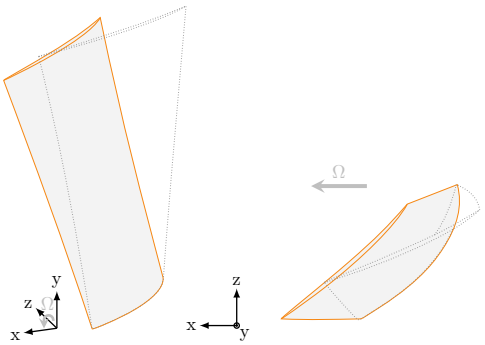

a side view **b** view from above

Figure 21. optimized transonic blade geometry

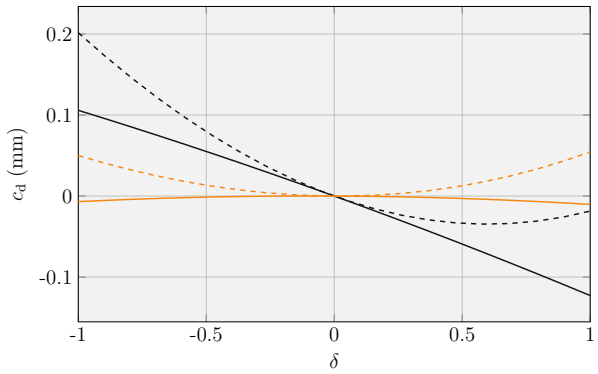

Figure 22. transonic blade's dynamic clearance: initial (——) and optimized (——) blade (non-linear computations are depicted with dashed lines)

6.2.3 Analysis

When looking at the wear map obtained for the optimized blade, see Fig. 23, areas where significant wear levels are predicted are still noticeable. In particular, one may note a 12-lobe wear pattern for $\Omega \in [155\,;160]$ Hz. Also, evidence of very high wear is found for $\Omega \in [258\,;280]$ Hz. For this latter angular speed range, predicted circumferential wear on the casing is twofold: some speeds feature a constant wear level along the casing circumference while for some other speeds an 8-lobe wear pattern may be found. By comparison with the wear map of the initial blade in Fig. 20, it is thus patent that wear patterns predicted for the optimized blades exhibit a larger number of lobes. This is an indication that the blade's dynamics may be driven by higher frequency modes. Consistently, the Campbell diagram depicted in Fig. 23 underlines that engine orders 12 and 8 intersect the first torsional mode frequency line in the vicinity of aforementioned angular speed ranges.

Overall, it seems that the optimization procedure of the transonic blade has indeed mitigated bending induced interactions.

However, undesirable torsion induced interactions are noticeable on Fig. 23. This brings into focus the relevance of the employed objective function. Indeed, the dynamic clearance is here solely computed for the first bending mode. It is possible that optimizing this quantity yields an increased dynamic clearance for other modes such as the first torsional mode thus increasing the blade sensitivity to structural contacts.

Because interactions may potentially arise for a large number of modes, the extension of the objective function to several bending and torsional modes could be costly from a computational standpoint. For the sake of efficiency, it is here proposed to keep a low-cost objective function related to the first bending mode only and to set more fitting parameter bounds based on empirical considerations.

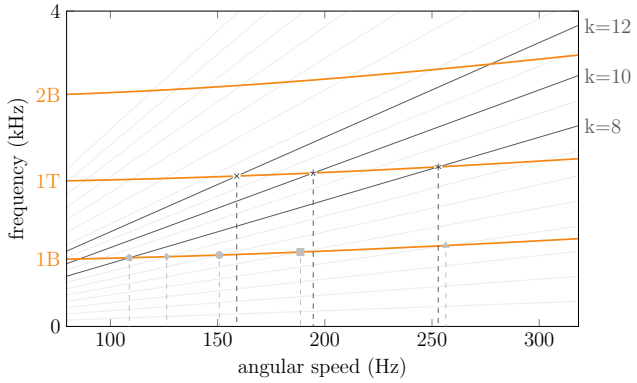

a Campbell diagram

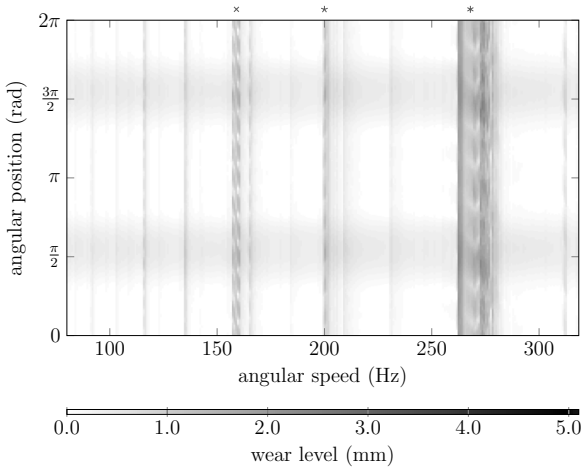

b wear map

Figure 23. optimized transonic blade analysis

6.3 Transonic blade with empirical parameters

From the previous optimization procedure, it can be observed that the optimized blade exhibits positive sweep and lean angles (parameters (17) and (18)). This goes against observations made following the optimization on the FFCS blade, where negative sweep and lean angles seemed to be beneficial in order to mitigate contact interactions. Therefore, this second optimization, carried out on the initial transonic blade, features updated parameter bounds to favor negative sweep and lean angles.

6.3.1 Optimization

Updated parameter bounds are given in Tab. 5. All other parameters are unchanged. The optimized geometry is depicted in Fig. 24, corresponding parameters are listed in Tab. 6. As expected, both sweep and lean angles are negative at the end of this second optimization. The dynamic clearance evolution obtained after the second optimization is shown in Fig. 25. The maximum dynamic clearance is reduced by 89.1 % compared to the initial blade, which is similar to the result of the first optimization.

parameter	lower limit	upper limit
sweep angle (**17**)	-30°	5°
lean angle (**18**)	-30°	5°
bowed distance (**19**)	0 mm	12 mm
stagger angle (**21**)	0°	45°

Table 5. second transonic blade optimization: optimization variables bounds

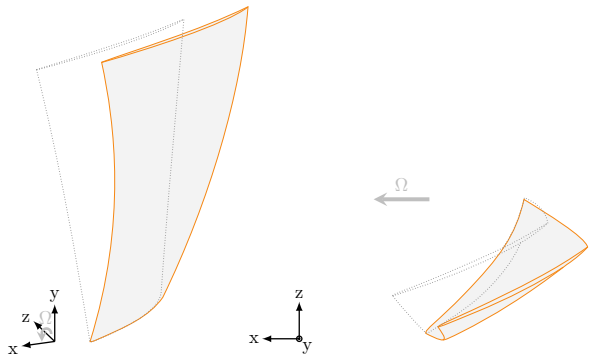

a side view **b** view from above

Figure 24. second optimized transonic blade geometry

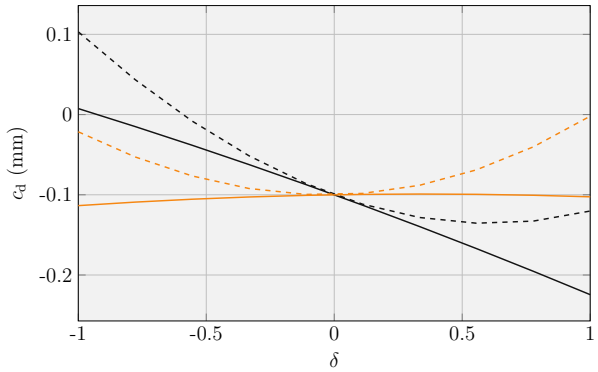

Figure 25. transonic blade's dynamic clearance: initial (——) and second optimized (——) blade (non-linear computations are depicted with dashed lines)

6.3.2 Analysis

The Campbell diagram of the optimized blade and the corresponding wear map are pictured in Fig. 26. Overall, wear levels are now very low with respect to those predicted in Figs. 20 and 23. The absence of distinct circumferential wear pattern at any angular speed suggests that there is no critical speed predicted with this second optimization. In particular, absolutely no wear

parameter	initial	optimized
hub radius (**15**)	177 mm	177 mm
blade height (**16**)	75 mm	75 mm
sweep angle (**17**)	**0.2**°	**-0.83**°
lean angle (**18**)	**4.20**°	**-8.41** °
bowed distance (**19**)	**1.22 mm**	**5.14 mm**
angle of incidence (**20**)	36°	36°
stagger angle (**21**)	**28.85**°	**25.88**°

Table 6. initial and optimized parameters for the second optimization of the transonic blade; optimization variables are indicated in bold

pattern that may be related to engine orders intersecting the first bending or the first torsional mode may be found. Thus, and contrary to what was observed in the first optimization of the transonic blade, the mitigation of bending induced interactions has not been made at the expense of interactions driven by higher frequency modes.

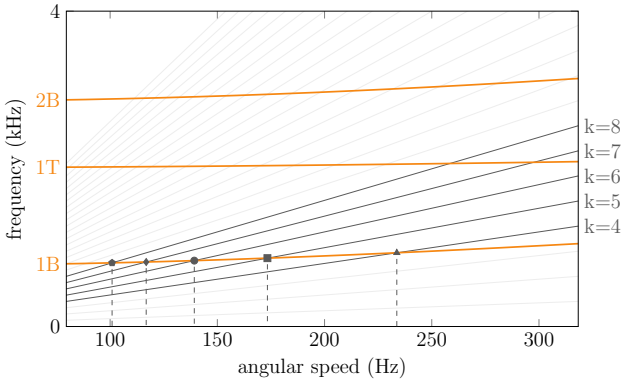

a Campbell diagram

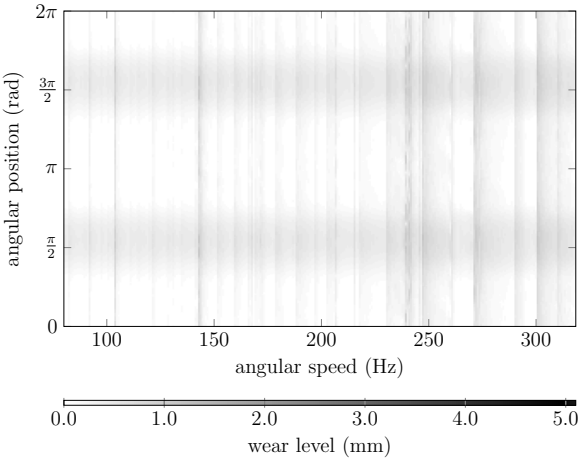

b wear map

Figure 26. second optimized transonic blade analysis

6.4 Discussion

The optimization of the transonic blade reveals that minimizing its dynamic clearance with respect to the first bending mode does indeed mitigate interactions involving the first bending mode. As a downside, the resulting blade may still exhibit high amplitudes of vibration along other modes. This is underlined by the first optimization for which wear patterns related to the first torsional mode are predicted, see Fig. 23. However, a wear map does not allow to discriminate transient events from the blade's steady state: it only provides a snapshot of the casing wear at the end of the interaction. In order to deepen the understanding of the blade's vibration, this section expands the scope of analysis to the blade's steady state and provides a displacement and stress analysis at critical speeds.

6.4.1 Steady state analysis

For each contact simulation presented in sections 6.2 and 6.3, a Fourier transform is applied on the blade's time response. Only the last 50 revolutions—over which it is assumed that a steady state has been reached—are accounted for. For each angular speed, computed spectra are stacked horizontally in order to draw an *interaction map*. These maps are depicted in Figs. 27, 28 and 29 for the initial transonic, the first optimized blade and second optimized blade with empirical parameters, respectively. The amplitudes are logarithmic, and the employed color code is identical for the three spectra, ranging form the same minimal amplitude a_{min} (in white) to the same maximal amplitude a_{max} (in black).

As mentioned above, the considered contact scenario features two symmetric privileged contact areas along the casing circumference. Outside of interaction areas, the blade dynamics is thus related to a synchronous excitation and the excitation frequency is twice the blade angular speed. This is the reason why even engine order lines ($k = 2, 4, 6$ and 8) are a privileged location for significant amplitudes of vibration on the three interaction maps.

When comparing predicted amplitudes for each blade in the vicinity of the first bending mode frequency line, a substantial improvement is observed from the initial blade to the first and second optimized blades: significant amplitudes predicted in Fig. 27 for the first bending mode vanish in Figs. 28 and 29. This is a confirmation that the contribution of the first bending mode in the blade's dynamic response has been significantly lowered due to the carried out optimization.

Evidence of significant amplitudes of vibration along the first torsional mode is found in Fig. 28 for the first optimized blade. Same as for the initial blade in Fig. 27, the intersection of several engine order lines with the first torsional mode frequency line features high amplitudes of vibration. For the first optimized blade however, it is noticeable that amplitudes of vibration have significanlty increased along the first torsional mode over the angular speed range $\Omega \in [258\,;280]$ Hz. The 8-lobe wear pattern observed in Fig. 23 is thus related to the blade's steady state response.

In the end, accounting for both Figs. 26 and 29, it can be said that the dynamic response of the second optimized blade features lower amplitudes of vibration—both for transient and steady state regimes—along the blade's first three free-vibration modes.

6.4.2 Displacement and stress analysis

The employed numerical strategy advantageously provides access to both the blade's displacement and stress fields at any time step. Accordingly, this section presents a detailed comparison of the results obtained at the critical speed 275.3 Hz for both the initial and the second optimized blade. Each blade's time response (leading edge radial displacement), spectrogram, displacement and stress fields at critical times are compared to highlight the increased performance—from a structural standpoint—of the optimized blade, see Figs. 30 and 31.

Time responses and spectrograms depicted in Figs. 30a and 31a underline fundamental differences between the two blades vibration behaviour subsequent to contact. Following the first contact events, the amplitudes of vibration of the initial blade increase to a point that the abradable coating is fully worn off. The predicted behaviour for the initial blade is actually divergent. The upper bound of the leading edge radial displacement visible in Fig. 30a for $t > 0.25$ s stems from the fact that the employed numerical methodology accounts for a perfectly rigid casing behind the abradable coating which makes it impossible for the amplitudes to increase indefinitely. The spectrogram highlights that the blade's dynamics is essentially driven by its first bending mode from contact initiation to the divergence. To the contrary, the second optimized blade features steady amplitudes of vibration after contact initiation, for $t \in [0\,;0.07]$ s. A small increase of amplitudes is predicted over a short amount of time. The associated spectrogram underlines that this increase relates to a contribution of the second bending mode only. The blade's response then stabilizes: a steady state is found for which the blade hits the casing twice per revolution with low amplitudes of vibration.

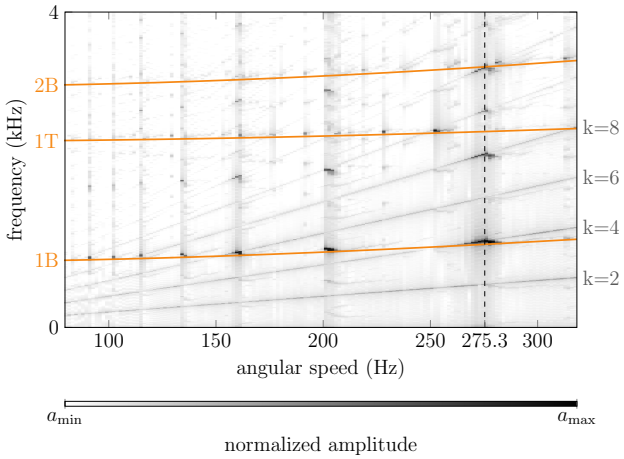

Figure 27. frequency spectra for the initial transonic blade with modal frequencies (——)

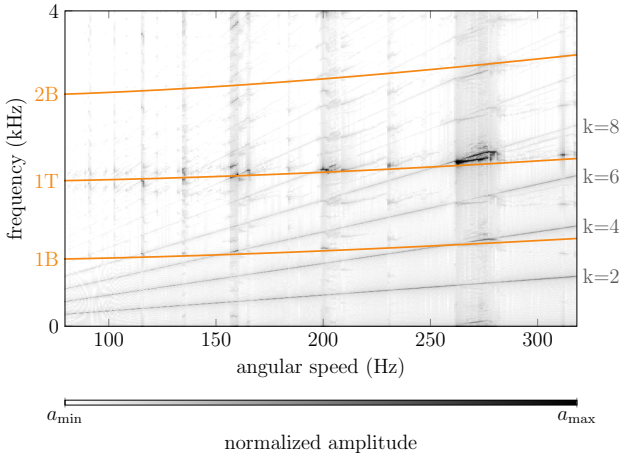

Figure 28. frequency spectra for the first optimized transonic blade with modal frequencies (——)

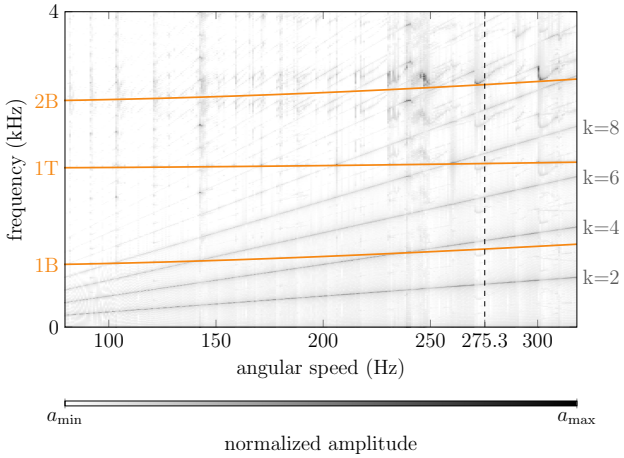

Figure 29. frequency spectra for the second optimized transonic blade with modal frequencies (——)

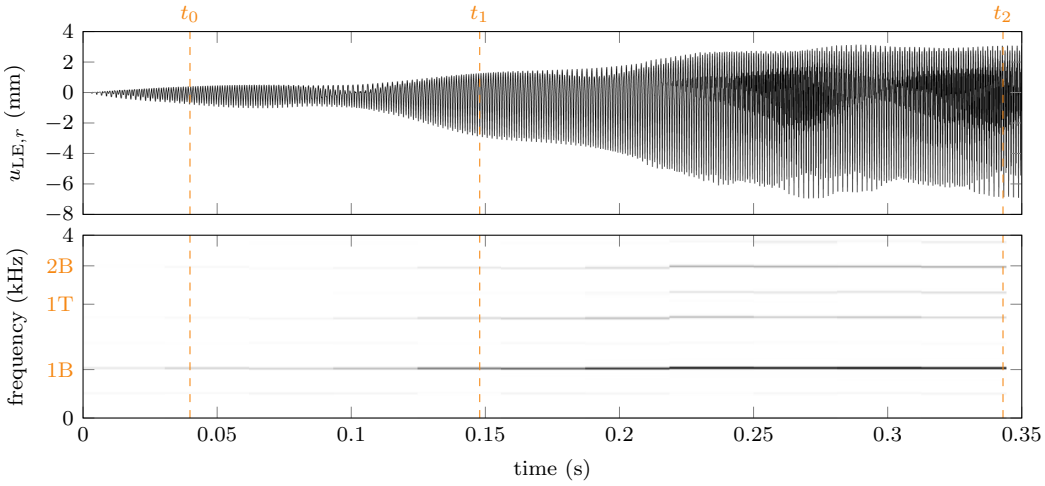

a radial displacement at the leading edge: time response and spectrogram

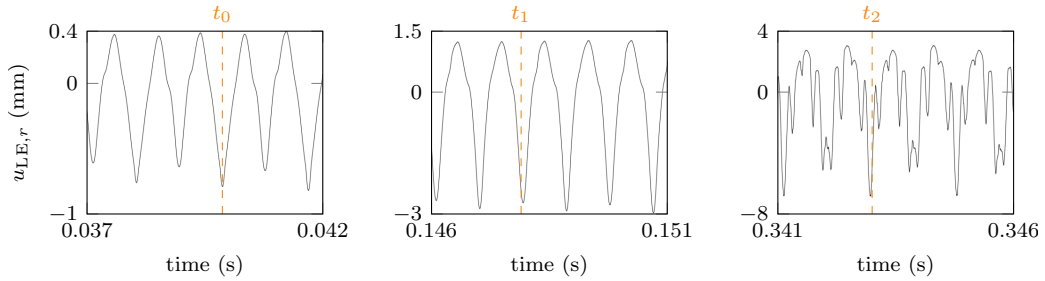

b radial displacement at the leading edge: zoom on time response

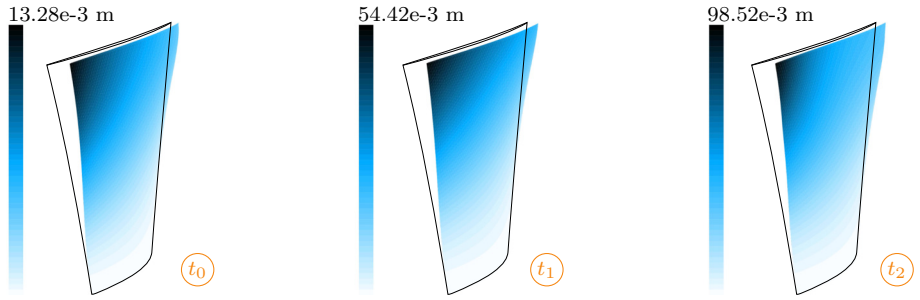

c displacement fields $u = \sqrt{u_r^2 + u_t^2 + u_z^2}$

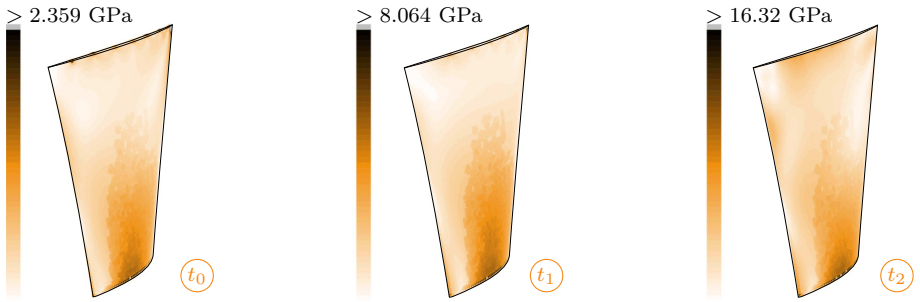

d stress fields

Figure 30. analysis of the initial transonic blade at 275.3 Hz

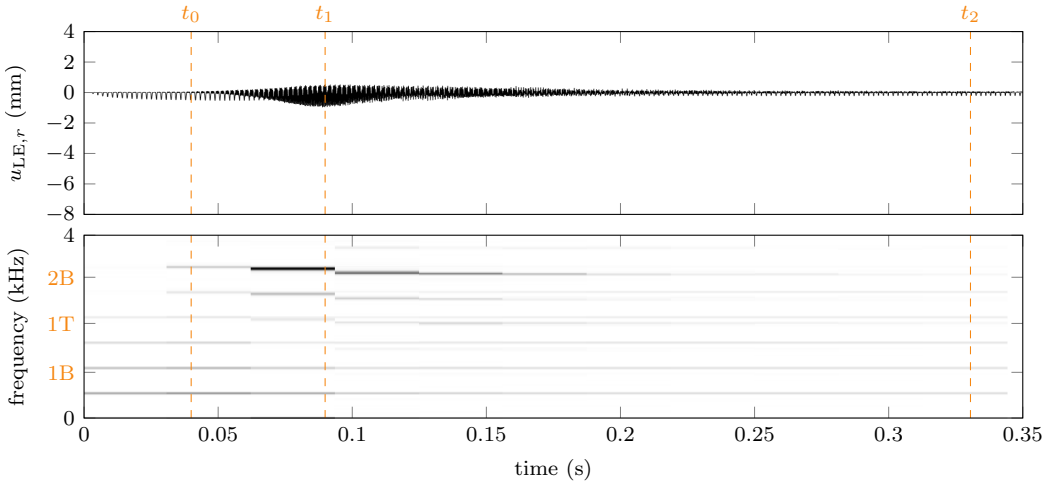

a radial displacement at the leading edge: time response and spectrogram

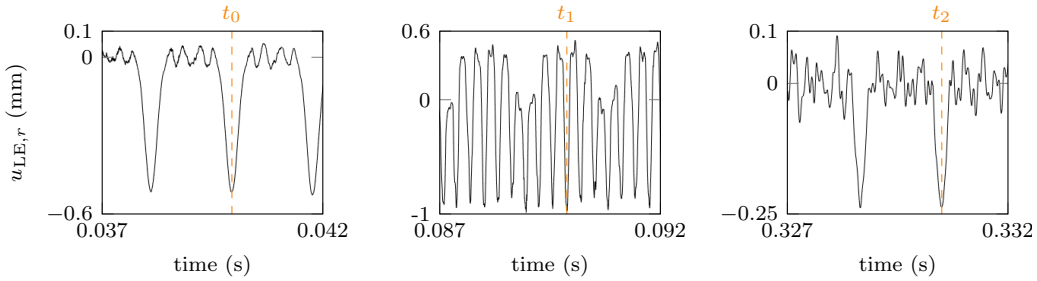

b radial displacement at the leading edge: zoom on time response

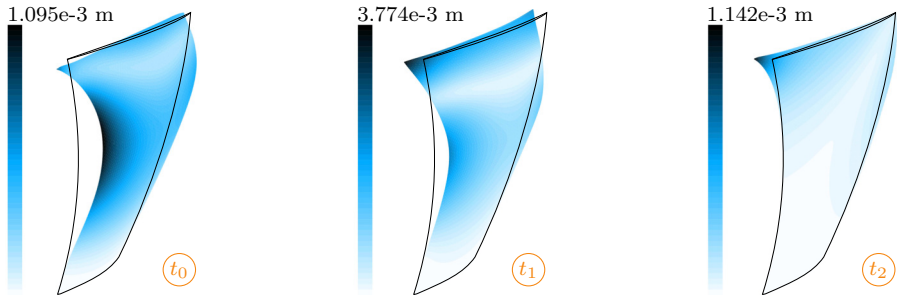

c displacement fields $u = \sqrt{u_r^2 + u_t^2 + u_z^2}$

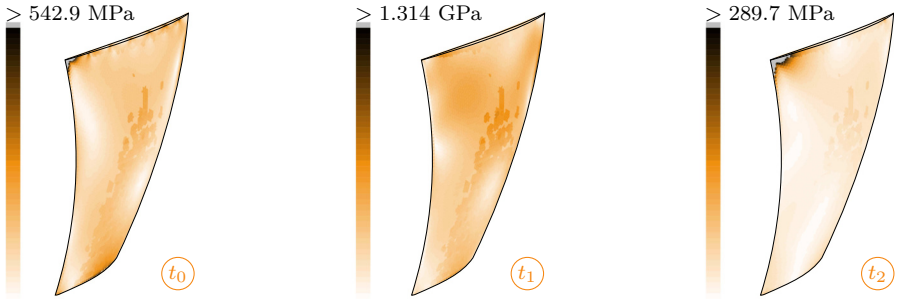

d stress fields

Figure 31. analysis of the second optimized transonic blade at 275.3 Hz

For each time response, three time steps are considered for further analysis of both displacement and stress fields: for both blades, t_0 corresponds to a few revolutions after contact is initiated, t_1 corresponds to the divergent motion of the initial blade and the maximum of amplitude of the second optimized blade. Finally, t_2 is the time for which the amplitude of vibration of the initial blade is maximum while the second optimized blade has reached a steady state. A zoom of the blade's time response in the vicinity of these three time steps is depicted for each blade in Figs. 30b and 31b. Displacement fields plotted for each of these time steps for the initial blade and the second optimized blade, respectively in Figs. 30c and 31c, indicate that both blades' largest displacements are located around the leading edge. For the second optimized blade however, the dominant second bending mode yields significant displacements at the blade tip and around mid-span, see t_0 and t_1 in Fig. 31c.

One may note that predicted displacements for the initial blade are very large: they are the same order of magnitude as the blade height for t_1 and t_2 in Fig. 30c. This is a clear indication that displacements and stresses cannot be analysed realisitically for $t \geq t_1$ with the employed strategy which is based on the use of linear finite element models. In reality, and similarly to what has already been experimentally observed on low-pressure compressor blades [34], the predicted divergent behaviour of the initial blade does yield large amplitudes of vibration which generate extremely high stresses within the blades and unavoidably leads to blade failure which goes beyond the scope of linear finite element models used in the employed numerical strategy. This explains the unrealistic stress values predicted for t_1 and t_2 within the initial blade in Fig. 30d. What is important however, is the fact that throughout the simulation, the amplitudes of vibration of the second optimized blade remain within an acceptable range for a linear finite element model. Results given in Figs. 31d are thus of interest and can be analyzed thoroughly. The optimized blade shows significantly lower stress levels, be it at t_0 with an eight-fold reduction (> 542.9 MPa), or during the increased response amplitude at t_1 with an almost two-fold reduction (> 1.314 GPa).

These results confirm that the proposed optimization procedure yields significant improvements in terms of the blade vibration response as it prevents the emergence of divergent motions following contact events. Numerical predictions for the second optimized transonic blade are in line with observations made for the FFCS blade. They suggest that negative sweep and lean angles are pertinent in order to reduce bending and torsion induced interactions. This seems to be an important result as it goes against conclusions drawn from blade optimization studies carried out from an aerodynamic standpoint. Indeed, recent investigations concluded that forward lean [35] and forward sweep [7] are desirable when considering aerodynamic performances.

A more systematic study is required in order to confirm the effect of each geometric parameter of a blade on its vibration response following contacts. Yet, the presented investigations indicate that the recent drive toward more efficient aircraft engines with a focus on clearance reduction—that unavoidably leads to more frequent blade/casing contact events—may imply to find a new balance between structural aspects and aerodynamics in the design process of bladed components.

7 Conclusion

This article presents an automated optimization procedure dedicated to the optimization of blades subject to structural contacts with the surrounding casing. An original parameterization of the blade geometry is proposed, it relies on the definition of three profiles and a stacking law with 49 independent parameters. The objective function relates to the notion of dynamic clearance, a quantity which describes the evolution of blade/casing clearance as the blade vibrates along a free vibration mode.

The procedure is tested on two different blades. It is demonstrated that the optimization procedure can reduce the dynamic clearance up to 90 %. The vibration response of both initial and optimized blades is compared by means of an in-house numerical strategy dedicated to the prediction of blade/casing structural contact events. The simulations focus on rubbing phenomena, which involve single blade vibration following contact events. Results feature in-depth analyses of the blade response over time including spectrograms, displacement fields and stress fields. Also, the combined analysis of frequency spectra and wear levels on the casing at the end of a simulation provide both transient and steady state related quantities for a thorough review of each blade's dynamics.

It is found that optimized blades feature significantly lower amplitudes of vibration following contacts. In particular, bending induced interactions vanish throughout the investigated angular speed range. These results confirm that dynamic clearance may be a relevant quantity to look at when assessing a blade sensitivity to structural contact. Additionally, it is evidenced that optimized blades also feature much lower stress levels and may thus be less prone to high cycle fatigue and crack initiation.

Overall, presented results provide insight on the relationship between the blades' 3D parameters and their sensitivity to structural contacts. In particular, for the investigated blade geometries, backward sweep and backward lean angles are

associated with reduced contact interactions compared to forward sweep and forward lean angles. This trend seems to be in contrast to aerodynamic recommendations, and a more systematic investigation will have to be performed on the necessary balance between aerodynamic and structural considerations for blade design. The present work is a step toward the inclusion of nonlinear structural criteria for the design of bladed components. The identification of dynamic clearance as a potentially relevant criterion to assess a blade sensitivity to contact offers a promising alternative to costly nonlinear numerical simulations.

Acknowledgment

This research was supported by the Fonds de Recherche du Québec – Nature et Technologies (FRQ-NT) and the Natural Sciences and Engineering Research Council of Canada (NSERC).

References

[1] Seo, S.-J., Choi, S.-M., and Kim, K.-Y., 2008. "Design Optimization of a Low-Speed Fan Blade with Sweep and Lean". In Proceedings of the Institution of Mechanical Engineers, Part A: Journal of Power and Energy, Vol. 222, pp. 87–92. doi:10.1243/09576509JPE410.

[2] Sieverding, F., Ribi, B., Casey, M., and Meyer, M., 2004. "Design of Industrial Axial Compressor Blade Sections for Optimal Range and Performance". *Journal of Turbomachinery,* **126**(2), pp. 323–331. doi:10.1115/1.1737782.

[3] Samad, A., and Kim, K. Y., 2008. "Multi-Objective Optimization of an Axial Compressor Blade". *Journal of Mechanical Science and Technology,* **22**(5), pp. 999–1007. doi:10.1007/s12206-008-0122-5.

[4] Sommer, L., and Bestle, D., 2011. "Curvature Driven Two-Dimensional Multi-Objective Optimization of Compressor Blade Sections". *Aerospace Science and Technology,* **15**(4), pp. 334–342. doi:10.1016/j.ast.2010.08.008.

[5] Goel, S., Cofer, J., and Singh, H., 1996. "Turbine Airfoil Design Optimization". In ASME 1996 International Gas Turbine and Aeroengine Congress and Exhibition, Vol. Volume 1: Turbomachinery, p. V001T01A055. 96-GT-158, doi:10.1115/96-gt-158.

[6] Chen, N., Zhang, H., Ning, F., Xu, Y., and Huang, W., 2006. "An Effective Turbine Blade Parametrization and Aerodynamic Optimization Procedure using an Improved Response Surface Method". In ASME Turbo Expo 2006: Power for Land, Sea, and Air, Vol. Volume 6: Turbomachinery, Parts A and B, pp. 1169–1180. GT2006-90104, doi:10.1115/gt2006-90104.

[7] Erler, E., Vo, H. D., and Yu, H., 2016. "Desensitization of axial compressor performance and stability to tip clearance size". *Journal of Turbomachinery,* **138**(3), p. 031006. doi:10.1115/1.4031865.

[8] Benini, E., 2004. "Three-Dimensional Multi-Objective Design Optimization of a Transonic Compressor Rotor". *Journal of Propulsion and Power,* **20**(3), may, pp. 559–564. doi:10.2514/1.2703.

[9] Razavi, S. R., Sammak, S., and Boroomand, M., 2017. "Multidisciplinary design and optimizations of swept and leaned transonic rotor". *Journal of Engineering for Gas Turbines and Power,* **139**(12), p. 122601. doi:10.1115/1.4037456.

[10] Pierret, S., Filomeno Coelho, R., and Kato, H., 2007. "Multidisciplinary and multiple operating points shape optimization of three-dimensional compressor blades". *Structural and Multidisciplinary Optimization,* **33**(1), Jan, pp. 61–70. doi:10.1007/s00158-006-0033-y.

[11] Ma, H., Wang, D., Tai, X., and Wen, B., 2015. "Vibration Response Analysis of Blade-Disk Dovetail Structure Under Blade Tip Rubbing Condition". *Journal of Vibration and Control,* **23**(2), pp. 252–271. doi:10.1177/1077546315575835.

[12] Batailly, A., Agrapart, Q., Millecamps, A., and Brunel, J.-F., 2016. "Experimental and numerical simulation of a rotor/stator interaction event within an industrial high-pressure compressor". *Journal of Sound and Vibration,* **375**, pp. 308–331. doi:10.1016/j.jsv.2016.03.016 - oai:hal-01342401.

[13] Schmiechen, P., 1997. "Travelling Wave Speed Coincidence". PhD thesis, University of London.

[14] Muszynska, A., 1986. "Whirl and Whip-Rotor/Bearing Stability Problems". *Journal of Sound and Vibration,* **110**(3), pp. 443–462. doi:10.1016/S0022-460X(86)80146-8.

[15] Sinha, S. K., 2013. "Rotordynamic analysis of asymmetric turbofan rotor due to fan blade-loss event with contact-impact rub loads". *Journal of Sound and Vibration,* **332**(9), pp. 2253–2283. doi:10.1016/j.jsv.2012.11.033.

[16] Hulme, C., Fiebiger, S., and Szwedowicz, J., 2015. "Axial compressor blade failure, design modification, and its validation". In Proceedings of the ASME Turbo Expo 2015 conference, Vol. Volume 7A: Structures and Dynamics, p. V07AT28A011. GT2015-43312, doi:10.1115/gt2015-43312.

[17] Batailly, A., Legrand, M., Millecamps, A., Cochon, S., and Garcin, F., 2014. "Redesign of a High-Pressure Compressor Blade Accounting for Nonlinear Structural Interactions". *Journal of Engineering for Gas Turbines and Power,* **137**(2), p. 022502. doi:10.1115/1.4028263 - oai:hal-01120158.

[18] Batailly, A., and Millecamps, A., 2016. "Minimising Clearance Consumption: a Key Factor for the Design of Blades Robust To Rotor/Stator Interactions ?". In ASME Turbo Expo 2016: Turbomachinery Technical Conference and Exposition, Vol. Volume 7A: Structures and Dynamics, p. V07AT32A011. GT2016-56721, doi:10.1115/GT2016-56721 - oai:hal-01618315.

[19] Pritchard, L. J., 1985. "An Eleven Parameter Axial Turbine Airfoil Geometry Model". In ASME 1985 International Gas Turbine Conference and Exhibit, Vol. Volume 1: Aircraft Engine; Marine; Turbomachinery; Microturbines and Small Turbomachinery, p. V001T03A058. 85-GT-219.

[20] Cho, S. Y., Yoon, E. S., and Choi, B. S., 2002. "A Study on an Axial-Type 2-D Turbine Blade Shape for Reducing the Blade Profile Loss". *KSME International Journal,* **16**(8), pp. 1154–1164. doi:10.1007/bf02984026.

[21] Ronald H., A., 2003. "Axial-Flow Compressor Blade Profiles". In *Axial-Flow Compressors*. ASME, ch. 4, pp. 59–76. doi:10.1115/1.801926.ch4.

[22] Reid, L., and Moore, R. D., 1978. Design and Overall Performance of Four Highly Loaded, High-Speed Inlet Stages for an Advanced High-Pressure Ratio Core Compressor. Tech. Rep. NASA TP-1337, NASA.

[23] Steinert, W., Eisenberg, B., and Starken, H., 1991. "Design and Testing of a Controlled Diffusion Airfoil Cascade for Industrial Axial Flow Compressor Application". *Journal of Turbomachinery,* **113**(4), pp. 583–590. doi:10.1115/1.2929119.

[24] Denton, J. D., and Xu, L., 2002. "The Effects of Lean and Sweep on Transonic Fan Performance". In ASME Turbo Expo 2002: Power for Land, Sea, and Air, Vol. Volume 5: Turbo Expo 2002, Parts A and B, pp. 23–32. GT2002-30327, doi:10.1115/GT2002-30327.

[25] Abramson, M. A., Audet, C., Couture, G., Dennis, Jr., J. E., Le Digabel, S., and Tribes, C. The NOMAD Project. Software available online : https://www.gerad.ca/nomad/.

[26] Abramson, M. A., Audet, C., Dennis, J. E., and Digabel, S. L., 2009. "OrthoMADS: A Deterministic MADS Instance with Orthogonal Directions". *SIAM Journal on Optimization,* **20**(2), jan, pp. 948–966. doi: 10.1137/080716980.

[27] Puri, R. S., and Morrey, D., 2011. "A Krylov–Arnoldi reduced order modelling framework for efficient, fully coupled, structural–acoustic optimization". *Structural and Multidisciplinary Optimization,* **43**(4), pp. 495–517. doi:10.1007/s00158-010-0588-5.

[28] Marwaha, G., and Kokkolaras, M., 2015. "System-of-systems approach to air transportation design using nested optimization and direct search". *Structural and Multidisciplinary Optimization,* **51**(4), pp. 885–901. doi:10.1007/s00158-014-1180-1.

[29] Ribes, A., and Caremoli, C., 2007. "Salomé Platform Component Model for Numerical Simulation". In 31st Annual International Computer Software and Applications Conference, Vol. 2, pp. 553–564. doi:10.1109/compsac.2007.185.

[30] Bogdonoff, S. M., and Bogdonoff, H. E., 1945. Blade Design Data for Axial-Flow Fan and Compressors. Tech. rep., NACA, USA.

[31] Denton, J., 1997. "Lessons from rotor 37". *Journal of Thermal Science,* **6**(1), pp. 1–13. doi:10.1007/s11630-997-0010-9.

[32] Batailly, A., Legrand, M., Millecamps, A., and Garcin, F., 2012. "Numerical-Experimental Comparison in the Simulation of Rotor/Stator Interaction Through Blade-Tip/Abradable Coating Contact". *Journal of Engineering for Gas Turbines and Power,* **134**(8), p. 082504. doi:10.1115/1.4006446 - oai:hal-00746632.

[33] Legrand, M., Batailly, A., and Pierre, C., 2012. "Numerical Investigation of Abradable Coating Removal in Aircraft Engines Through Plastic Constitutive Law". *Journal of Computational and Nonlinear Dynamics,* **7**(1), p. 011010. doi:10.1115/1.4004951 - oai:hal-00627526.

[34] Millecamps, A., Brunel, J.-F., Dufrenoy, P., Garcin, F., and Nucci, M., 2009. "Influence of Thermal Effects During Blade-Casing Contact Experiments". In ASME 2009 International Design Engineering Technical Conferences and Computers and Information in Engineering Conference, Vol. Volume 1: 22nd Biennial Conference on Mechanical Vibration and Noise, Parts A and B, pp. 855–862. DETC2009-86842, doi:10.1115/detc2009-86842 - oai:hal-01223060.

[35] Benini, E., and Biollo, R., 2007. "Aerodynamics of swept and leaned transonic compressor-rotors". *Applied Energy,* **84**(10), pp. 1012–1027. doi:10.1016/j.apenergy.2007.03.003.